LANGMUIR

pubs.acs.org/Langmuir Article

Design of Pd-Decorated $SrTiO_3$/BiOBr Heterojunction Materials for Enhanced Visible-Light-Based Photocatalytic Reactivity

Mary O. Olagunju, Elsayed M. Zahran, Elnaz Zeynaloo, Dharmendra Shukla, Joshua L. Cohn, Bapurao Surnar, Shanta Dhar, Leonidas G. Bachas, and Marc R. Knecht*

Cite This: *Langmuir* 2021, 37, 11986–11995 Read Online

ACCESS | Metrics & More | Article Recommendations | Supporting Information

ABSTRACT: The development of photocatalytic materials that exploit visible light is imperative for their sustainable application in environmental remediation. While a variety of approaches have been attempted, facile routes to achieve such structures remain limited. In this contribution, a direct route for the production of a $SrTiO_3$/BiOBr/Pd heterojunction is presented that employs a low temperature, sustainable production method. The materials were produced in a two-step process wherein BiOBr nanoplates are fabricated in the presence of the $SrTiO_3$ nanospheres, generating a highly integrated composite material. Pd nanoparticle surface decoration was subsequently employed to facilitate and enhance charge separation lifetimes to optimize reactivity. The structures were fully characterized via a suite of approaches to confirm the final material composition and arrangement. Their reactivity was explored for the degradation of both colored and colorless model environmental pollutants, where the $SrTiO_3$/BiOBr/Pd demonstrated significant reactivity using visible light, leading to substrate degradation in <10 min in some cases. The enhanced reactivity was attributed to the significant integration between materials, facilitating electron transfer. Such studies provide key information for the development of new materials with optimized visible-light-driven photocatalytic reactivity for sustainable environmental remediation.

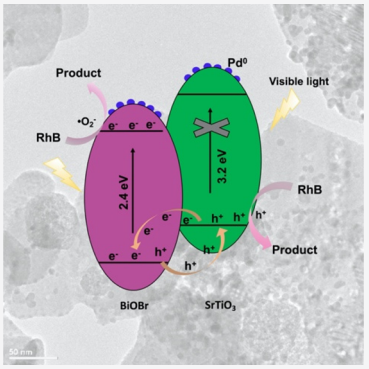

INTRODUCTION

Semiconductor-based photocatalysis has been the subject of intense research activity for several decades, offering the promises of sustainable approaches to drive chemical transformations.[1] Such reactions include water splitting for energy production, a variety of organic reactions for molecular transformation, decomposition processes for environmental remediation, etc.[2−4] All of these reactions are critically important to achieve green-based methods for chemical processes; however, the application of these approaches remains challenging due to the lack of highly functional materials, especially in the visible range of the electromagnetic spectrum. The use of visible light is critically important for harnessing a broader swath of the solar spectrum for optimized reactivity.[5] Many commonly applied photocatalysts such as TiO_2 and ZnO require UV-based light for photocatalytic reactivity and are not able to be activated by the lower energy photons of visible light.[6] Elegant approaches for the production of complex semiconductor materials have been developed to tune the optical properties of the semiconductors to be activated by visible light, including doping methods and complex heterostructure formation.[7,8] While these materials can be activated by visible light, their harsh synthetic conditions or difficult production schemes limit their widespread application, especially for energy harvesting and environmental remediation catalysis that require large quantities of sustainably sourced materials. As such, new and facile approaches for material production with optimal reactivity driven via visible light are required. Ideally these methods could be amenable for large batch material production with minimal energy input, which would be important for their long-term and sustainable production.

Strontium titanate ($SrTiO_3$) has recently emerged as an intriguing semiconductor photocatalyst. This n-type metal oxide semiconductor has similar properties to TiO_2,[9] where it has been used for photocatalytic degradation of dyes as model organic pollutants,[4,10,11] water splitting,[2,3,12] and NO removal.[13] Although its properties are attractive, its large band gap of 3.2 eV facilitates charge recombination of electron−hole pairs, leading to low photocatalytic efficiency.[6] Furthermore, it requires UV light for reactivity, not making it amenable to visible-light activation. Efforts to increase the photocatalytic activity of $SrTiO_3$ include doping the lattice structure of the material,[7] controlling the morphology of the particle,[14] and the incorporation of secondary components as a heterojunc-

Received: June 7, 2021
Published: October 5, 2021

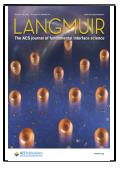

https://doi.org/10.1021/acs.langmuir.1c01537
Langmuir 2021, 37, 11986−11995

tion.[8,15] The latter method, heterojunction design, is attractive as it can reduce the recombination rate of the electron−hole pairs, thereby increasing the photocatalytic efficiency of the material. It could also be designed to activate the materials for photocatalysis using visible light; however, the reactivity of the composite materials is highly dependent upon the composition of the secondary p-type semiconductor component. For instance, Ji et al. synthesized a Z-scheme heterojunction of $Ag_3PO_4/Ag/SrTiO_3$ for the degradation of volatile organic compounds.[15] The composite showed strong visible-light response and improved catalytic activity compared to the Ag_3PO_4 and $SrTiO_3$ components individually. This team also constructed a $Cu_xO/SrTiO_3$ heterostructure for visible-light photocatalytic degradation of toluene, benzene, and xylene, which also demonstrated a higher reactivity as compared to the individual components.[16] This suggests that $SrTiO_3$ may prove to be an ideal component in heterojunctions where judicious selection of the p-type component could lead to optimized visible-light reactivity.

A model p-type semiconductor system, bismuth oxyhalides (BiOX; X = Cl, Br, or I), has an open crystalline structure, providing sufficient space to induce internal static electric fields.[17,18] As a result of this unique open structure, it facilitates exciton lifetime and thus the photocatalytic reactivity. More specifically, BiOBr is visible-light active with a band gap of 2.92 eV, making it an ideal photocatalyst to harness a broad range of solar energy.[19] Taken together, these properties make BiOBr a unique system for integration with $SrTiO_3$, thus forming a p−n heterojunction, which is anticipated to not only enhance reactivity but also optimize the composite material for activity with visible light (Scheme 1). For instance, Kanagaraj et al.

Scheme 1. Visible-Light-Activated Photocatalytic Mechanism for the $SrTiO_3$/BiOBr/Pd Materials

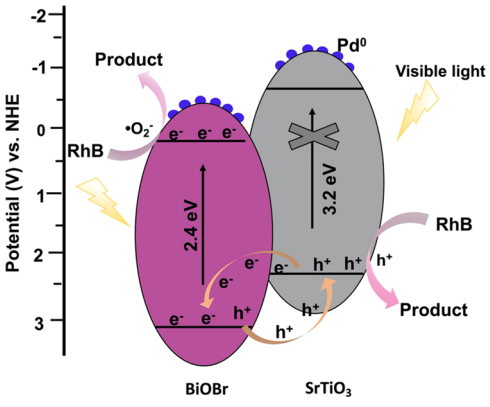

have synthesized a nanocube-shaped $SrTiO_3$/BiOBr (STO/BiOBr) heterojunction with different weight percents of $SrTiO_3$ for the degradation of organic dyes under visible-light irradiation. The 10% STO/BiOBr composite showed the highest reactivity over bare $SrTiO_3$ and BiOBr, decoloring the dyes within 30−60 min.[20] Xia et al. fabricated a $SrTiO_3/Bi_5O_7I$ nanocomposite via thermal decomposition for Rhodamine B dye (RhB) degradation. Specifically, the 30 wt % STO/Bi_5O_7I material showed optimal photocatalytic degradation, where 89.6% of the dye was degraded over 150 min. The reactivity was ∼4 times and 12.5 times higher than that of bare Bi_5O_7I and $SrTiO_3$, respectively.[21]

In this work, we present a direct and facile route for the production of a $SrTiO_3$/BiOBr heterojunction, which demonstrated optimized photocatalytic reactivity for the degradation of model organic environmental pollutants. Specifically, RhB dye, phenol, and nitrobenzene were chosen to illustrate photocatalytic degradation capabilities of both colored and colorless substrates. The composite was decorated with Pd^0 particles that enhanced charge separation lifetimes and, consequently, the overall reactivity. Once prepared, the materials were fully characterized via transmission and scanning electron microscopies (TEM and SEM, respectively), high-resolution TEM with energy-dispersive spectroscopy (EDS) elemental mapping, X-ray photoelectron spectroscopy (XPS), powder X-ray diffraction (XRD), and UV−vis diffuse reflectance spectroscopy (DRS). These methods confirmed heterojunction formation of the anticipated compositions and material arrangement where production of large-scale quantities of the materials could be possible. Once prepared, the reactivity of the heterojunction structure was examined to confirm changes in the observed reactivity by the photocatalytic degradation of model organic pollutants, including both colored and colorless species. The analysis demonstrated that both the $SrTiO_3$/BiOBr and $SrTiO_3$/BiOBr/Pd systems were readily activated using visible light where the palladized materials were significantly more reactive. Furthermore, the composite structures demonstrated enhanced reactivity over the individual $SrTiO_3$ and BiOBr system due to the heterojunction that allowed for enhanced charge separation lifetimes. This is especially true for the $SrTiO_3$ material that was unreactive under visible-light irradiation. Taken together, these results provide direct and facile routes to the production of complex heterostructured materials for enhanced photocatalytic reactivity under visible light, which could be adapted to a variety of different photocatalytic systems and reactions.

MATERIALS AND METHODS

Chemicals. $SrCl_2$ (>99%), bismuth(III) nitrate hydrate, ammonium metavanadate, and Rhodamine B were purchased from Alfa Aesar. $TiCl_4$ (99%) and phenol were acquired from Millipore, NaOH was from Acros Organics, potassium bromide was purchased from J.T. Baker, and palladium(II) acetate was purchased from STREM Chemicals. Tetrachloro-*m*-xylene (TCMX) was purchased from AccuStandard. Hexane (64%) was acquired from EMD Millipore, and 200 proof ethanol was supplied from Pharmaco-Aaper. All chemicals were used as received. High-purity deionized water (18.2 MΩ·cm) was used for all experiments.

Photocatalyst Synthesis. *Synthesis of $SrTiO_3$.* $SrTiO_3$ was synthesized through a modified sonication-based synthesis, building upon previous precedent.[22,23] For all solutions and syntheses, the flasks were kept under Ar gas, and all of the water (∼250 mL) was pretreated, which included the addition of ∼3 mg of NaOH to make it basic (pH ∼ 11.9) and boiled at 100 °C for 30 min. This was done to remove any trace CO_2 to prevent formation of metal carbonates. In a typical procedure, 0.2 M $SrCl_2{\cdot}6H_2O$ was diluted in 50 mL of H_2O, while 2.19 mL of 0.2 M $TiCl_4$ was diluted in 50 mL of ethanol. These two solutions were then combined, and the pH was increased to ≥13 using a minimal amount of aqueous concentrated NaOH. The reaction was then irradiated using a high-intensity sonicator (Q Sonica Q700, 2.5 cm diameter, 20 kHz, 30 amp) for 45 min. Once finished, the precipitate was collected via centrifugation and then washed three times each with water, dilute formic acid (∼0.01 M), dilute HCl (0.01 M), and ethanol. The powder material was finally dried at 60 °C in a vacuum oven overnight.

Synthesis of $SrTiO_3$/BiOBr. The $SrTiO_3$/BiOBr material was synthesized using a modified procedure.[20] In separate flasks, 790 mg of $Bi(NO_3)_3 \bullet xH_2O$ and 79 mg of the prepared $SrTiO_3$ powder were suspended in 180 mL of ethylene glycol and bath sonicated. Such masses were selected to result in a 10 wt % loading of $SrTiO_3$

https://doi.org/10.1021/acs.langmuir.1c01537
Langmuir 2021, 37, 11986−11995

with respect to the $Bi(NO_3)_3$ materials. Separately, 476 mg of KBr was dissolved in 20 mL of water. The KBr solution was then added into the reaction suspension and sonicated. The mixture was bath sonicated for 20 min and then heated at 120 °C overnight where the white product was finally washed with water and ethanol several times and dried in a 60 °C vacuum oven overnight.

Pd Deposition. Pd was deposited on the surface of the $SrTiO_3$/BiOBr catalyst using standard methods.[24] For this, 100 mg of the prepared $SrTiO_3$/BiOBr was dispersed in 70 mL of ethanol and then sonicated for 3 min. Once completed, 8 mg of $Pd(OOCCH_3)_2$ was added to the mixture, which was then sonicated for 30 s. The mixture was left to stir in the dark overnight at room temperature. Once completed, the product was washed and filtered several times with ethanol and dried in a 60 °C vacuum oven overnight.

Photocatalytic Experiments. Photocatalytic experiments were performed with a Sol 1A Class ABB 94061A solar simulator (Newport Corporation, USA) using a 1000-W xenon lamp with a 100 mW cm^{-2} power output. The distance between the light source and the top of the reaction solution was ∼15 cm. The photocatalytic activity of the metal oxide catalyst was studied by monitoring the degradation of Rhodamine B (RhB), phenol, and nitrobenzene contaminants with a UV cut off filter of <400 nm.

Rhodamine B Dye Degradation. For RhB dye degradation photocatalysis, 20 mg of catalyst was suspended in 20 mL of a 10 mg/L dye solution in water. After stirring in the dark for 30 min, the suspension was irradiated with a UV cut off filter. At selected time points, 600 μL aliquots were extracted and centrifuged to remove any semiconductor materials in the sample. The supernatant was then quantitated using UV−vis spectroscopy (Shimadzu UV-2600 spectrophotometer).

Phenol Degradation. For phenol degradation, 20 mg of the catalyst was suspended in 20 mL of an aqueous 10 ppm phenol solution and sonicated for 5 min. The mixture was left to stir in the dark for 30 min and then irradiated with light for 3 h with a UV cut off filter. During the reaction, 900 μL aliquots were obtained at selected time intervals and centrifuged to pellet and remove the particles, after which the species in the supernatant were quantified using high-performance liquid chromatography (HPLC).

Nitrobenzene Degradation. For the degradation of nitrobenzene, 20 mg of the catalysts was suspended in 20 mL of an aqueous 20 ppm nitrobenzene solution. The system was bath sonicated for ∼3 min to suspend the photocatalytic materials. The mixture was left to stir in the dark for 30 min and then irradiated under a solar simulator for 4 h with a UV cut off filter of <400 nm. Similar to the prior reactions, 500 μL aliquots were removed to monitor the reaction progress at specific times. These aliquots were extracted in 500 μL of hexane and shaken vigorously for 20 min to ensure complete substrate extraction. Once finished, 90 μL of the top layer was added with 10 μL of 10 μg/mL TCMX (internal standard) for GC−MS analysis.

Characterization. Crystallographic data were obtained for all photocatalyst samples with a Phillips MRD X'Pert X-ray diffractometer using Cu Kα radiation. SEM images were obtained with an FEI XL-30 microscope operating at 20 kV. Samples for the SEM analysis were prepared by dispersing the $SrTiO_3$/BiOBr-based materials in ethanol and drop-casting 15 μL onto an aluminum stub. Low-resolution TEM was performed with a JEOL JEM-1400 operating at 80 kV, while HRTEM images were obtained using a Tecnai F30 by FEI operating at 300 kV. EDS analysis was conducted by employing an Octane Elite T-55 detector (EDAX). For all TEM analyses, the samples were prepared by drop-casting 4 μL of dispersed sample in ethanol onto a carbon-coated Cu TEM grid. To characterize material dimensions, measurement of the particle diameter ($SrTiO_3$ and Pd) or plate thickness (BiOBr) was performed on >100 different material samples.

The samples were allowed to dry completely in a desiccator. XPS characterization was performed using a PHI 5000 Versa Probe II equipped with a focused monochromatic Al Kα source. A steady-state/transient fluorescence spectrometer (Edinburgh/FL920) equipped with a Ge detector was used to detect the recombination and lifetime of the photogenerated charge in the composite. The photocurrent measurements were carried out with a solar simulator (Oriel Instruments, Newport Corporation) where a high-power mercury−xenon lamp (300 W) was employed as a light source. The data were collected using an electrochemical workstation PARSTAT 2273 with the PowerSuite software version 2.40 (EG&G Princeton Applied Research, Oak Ridge, TN). Impedance studies were performed with an Autolab potentiostat PGSTAT128N controlled by NOVA 2.1.2 electrochemical software. Elemental analysis of the materials was performed using an Agilent 7900 inductively coupled plasma mass spectrometer. Total organic compound (TOC) analysis was performed with a Shimadzu TOC-L CPH. All UV−vis absorption spectra were recorded on a Shimadzu UV-2600 spectrophotometer. Nitrobenzene reaction progress was monitored by GC−MS (Agilent 5975C GC/MS with an HP-5MS column: 30 m length, 0.250 mm ID, 0.25 μm film thickness, Santa Clara, CA) using TCMX as an internal standard. HPLC analysis was performed with a Dionex Ultimate 3000 liquid chromatography system with an ultimate 3000 pump including a diode array detector (DAD 3000). The separation was achieved with a reverse-phase Eclipse plus C18 column (3.2 μm, 4.6 × 100 mm). The mobile phase was 70% H_2O/30% acetonitrile with a flow rate of 1 mL/min at 25 °C where the system was monitored at 270 nm.

RESULTS AND DISCUSSION

Material Synthesis. $SrTiO_3$ is a UV-active semiconductor with a large band gap of 3.2 eV, while BiOBr is visibly active with a band gap of 2.5−2.9 eV (Scheme 1).[25,26] Due to the valence and conduction band positions of the two oxides, it is anticipated that enhanced charge separation lifetimes could be achieved under visible-light activation, leading to enhanced reactivity. To examine this capability, a $SrTiO_3$/BiOBr composite was synthesized by first producing the $SrTiO_3$ material via a sonication-based approach. This was achieved using prior methods,[27] where complete characterization of the individual $SrTiO_3$ materials was fully described previously, resulting in the formation of spherical structures of ∼52 nm. Once prepared, the heterojunction was generated through the addition of bismuth(III) nitrate and potassium bromide to the semiconductor materials. This resulted in the fabrication of the BiOBr sheets that directly interacted with the $SrTiO_3$ nanoparticles. Note that the individual BiOBr nanosheets were previously studied.[24] For heterojunction formation, a 10 wt % $SrTiO_3$ value was selected as prior studies indicated that this amount resulted in maximal photocatalytic reactivity.[20] It is important to note that BiOBr was not prepared separately and subsequently added to $SrTiO_3$; however, the second oxide is grown directly in the mixture with the $SrTiO_3$ materials. This is anticipated to facilitate significant interactions between the two oxides that are critically important to enhance charge separation. Finally, to optimize the photocatalytic activity of the composite, Pd nanoparticles were surface decorated onto the composite materials. For this, the $SrTiO_3$/BiOBr heterojunction was dispersed in ethanol with $Pd(OOCCH_3)_2$ overnight, resulting in deposition of the zerovalent metal materials on the oxide surface. In this case, the Pd cocatalysts are envisioned to facilitate charge separation lifetimes and electron transfer reactions for radical formation in solution. A loading of 4 wt % Pd was selected to be consistent with previously published materials that demonstrated significant photocatalytic reactivity.[24]

To probe the overall morphology and arrangement of the inorganic materials, electron microscopy was employed to image the structures. Figure 1 presents the SEM images of the $SrTiO_3$/BiOBr materials before (Figure 1a) and after (Figure 1c) Pd nanoparticle deposition. From the SEM images, both

https://doi.org/10.1021/acs.langmuir.1c01537
Langmuir 2021, 37, 11986−11995

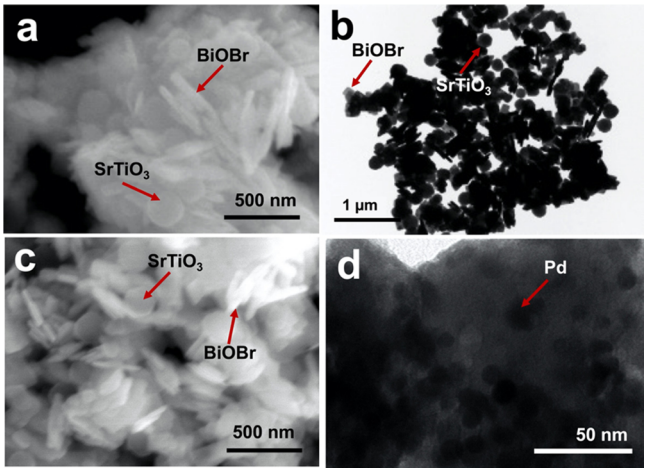

Figure 1. Low-resolution electron micrographs of the $SrTiO_3$/BiOBr materials (a and b) before and (c and d) after Pd nanoparticle deposition. Parts (a and c) present SEM images, while parts (b and d) present TEM images.

the BiOBr nanoplates and $SrTiO_3$ nanospheres are clearly evident, as indicated in the figure. When comparing the same sample after Pd nanoparticle deposition, no significant changes were noted in the materials. Such observations were anticipated as Pd nanoparticle production is unlikely to have any effect on the oxide structure, consistent with prior studies of $SrTiO_3$ and BiOBr.[24,27,28] In addition, the metallic materials are likely to be sufficiently small to hamper observation via SEM.

To examine the smaller-sized materials in the ternary composite structure, low-resolution TEM analysis was performed on the bare (Figure 1b) and Pd-coated $SrTiO_3$/BiOBr materials (Figure 1d). For the materials prior to Pd nanoparticle deposition, the BiOBr plates were evident where the corners of these materials were rounded. Small spherical structures are indicated in the image, arising from $SrTiO_3$, which were integrated onto the BiOBr nanoplates; however, higher magnification imaging is required to fully resolve the individual components. Figure 1d shows the same structures after Pd nanoparticle deposition where smaller spherical metal nanoparticles were evident on the heterojunction surface. To determine the Pd wt % deposited in the sample, inductively coupled plasma mass spectrometry (ICP-MS, Supporting Information, Figure S1) was performed, which indicated a 4% Pd loading on the $SrTiO_3$/BiOBr materials. Such a value correlates well with the initial amount of Pd added to the system (4 wt %).

While low-resolution TEM imaging provides a general structure for the $SrTiO_3$/BiOBr/Pd materials, higher magnification imaging is required to fully resolve the composite material morphology. To provide a more intricate level of structural understanding, high-resolution TEM (HR-TEM) imaging of the materials was performed where an image of the heterostructure is presented in Figure 2. In this analysis, thin and transparent BiOBr nanoplates are evident with $SrTiO_3$ nanospheres and Pd nanoparticles (smaller spheres) deposited on the plates. As anticipated from the synthetic process, the Pd nanoparticles were deposited on both the $SrTiO_3$ and BiOBr surfaces. From this analysis, the $SrTiO_3$ nanospheres demonstrated an average diameter of 52 ± 14 nm, while the Pd nanoparticles had an average size of 9.5 ± 6.1 nm. The

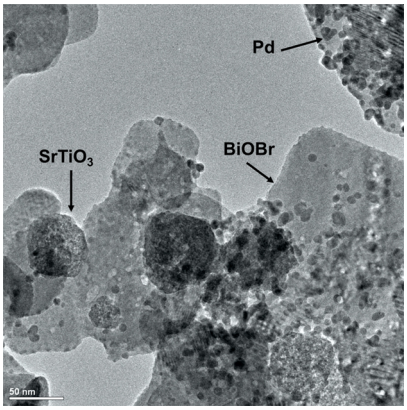

Figure 2. High-resolution TEM analysis of the $SrTiO_3$/BiOBr/Pd heterojunction.

average plate thickness for the BiOBr component was 37 ± 15 nm. In general, all the components of the heterojunction materials were well integrated, allowing for efficient electron transfer processes to enhance charge separation lifetimes.

To further verify the composition and component arrangement of the heterojunction material, high-angle annular dark-field (HAADF) STEM imaging with EDS mapping was done on the $SrTiO_3$/BiOBr/Pd structures (Figure 3). More specifically, Figure 3a presents the dark-field STEM image of the individual structure that was analyzed. Mapping of the Bi, Br, and O elements that arise from the BiOBr component is shown in Figure 3b–d, which confirmed the composition of the platelike material. Figure 3d–f presents regions where O, Sr, and Ti were observed, respectively, which arise from the $SrTiO_3$ nanospheres that were incorporated along the BiOBr nanoplate. As anticipated, both Sr and Ti were collocated at the same points, correlating with the $SrTiO_3$ materials. Finally, Figure 3g presents the mapping analysis for the Pd nanoparticles, which demonstrated that the noble metal material was integrated in small domains over both oxide components. In general, such mapping analysis was fully consistent with the HRTEM image of Figure 2, consistent with the close integration of the individual components in the heterojunction.

To further characterize the $SrTiO_3$/BiOBr/Pd materials, powder XRD and XPS analyses were done to confirm the material composition. Figure 4a presents the XRD patterns for $SrTiO_3$ and $SrTiO_3$/BiOBr structures. The major diffraction peaks for $SrTiO_3$ were evident at $°2\theta$ = 22.4, 32, 39.74, 46, 57.4, 67.16, and 76.7 corresponding to (100), (110), (111), (200), (211), (220), and (310) reflections of the oxide material (JCPDS file 73-0661).[27] After incorporation of BiOBr to generate the heterojunction, diffraction peaks associated with both oxides ($SrTiO_3$ and BiOBr) were evident in the sample. In addition to the SrTiO3 peaks noted above, major diffraction peaks of BiOBr were observed at $°2\theta$ = 25.2, 32.16, 46.2, and 57.2, corresponding to the (101), (110), (200), and (212) reflections (JCPDS file 09-0393).[18] The patterns reveal well-resolved peaks, indicating a highly crystalline material of the anticipated composition. XRD analysis of the ternary composite $SrTiO_3$/BiOBr/Pd structures was identical to the Pd-free materials. No diffraction peaks associated with the noble metal component were observed due to their low percent composition of the final material sample.

To further explore the structural composition of the materials, XPS analysis was performed on $SrTiO_3$/BiOBr/Pd.

https://doi.org/10.1021/acs.langmuir.1c01537
Langmuir 2021, 37, 11986–11995

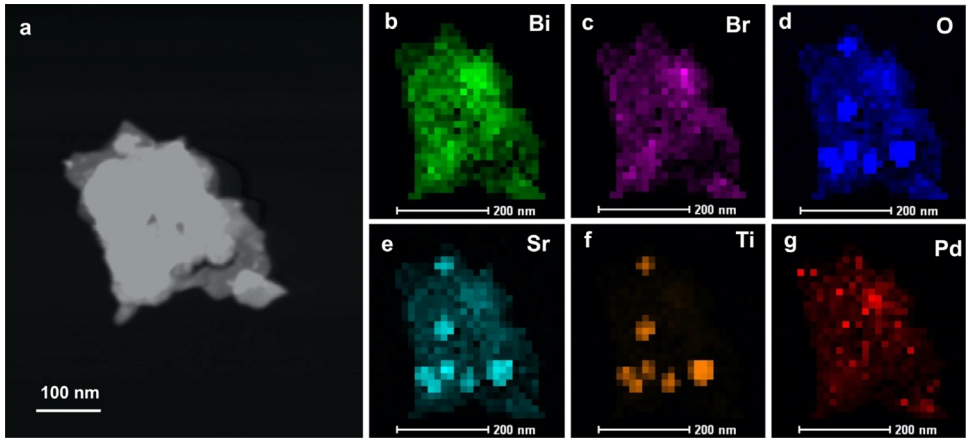

Figure 3. HAADF STEM and EDS mapping analysis. Part (a) presents the HAADF STEM image of the $SrTiO_3$/BiOBr/Pd materials where the individual elemental maps for (b) Bi, (c) Br, (d) O, (e) Sr, (f) Ti, and (g) Pd are shown.

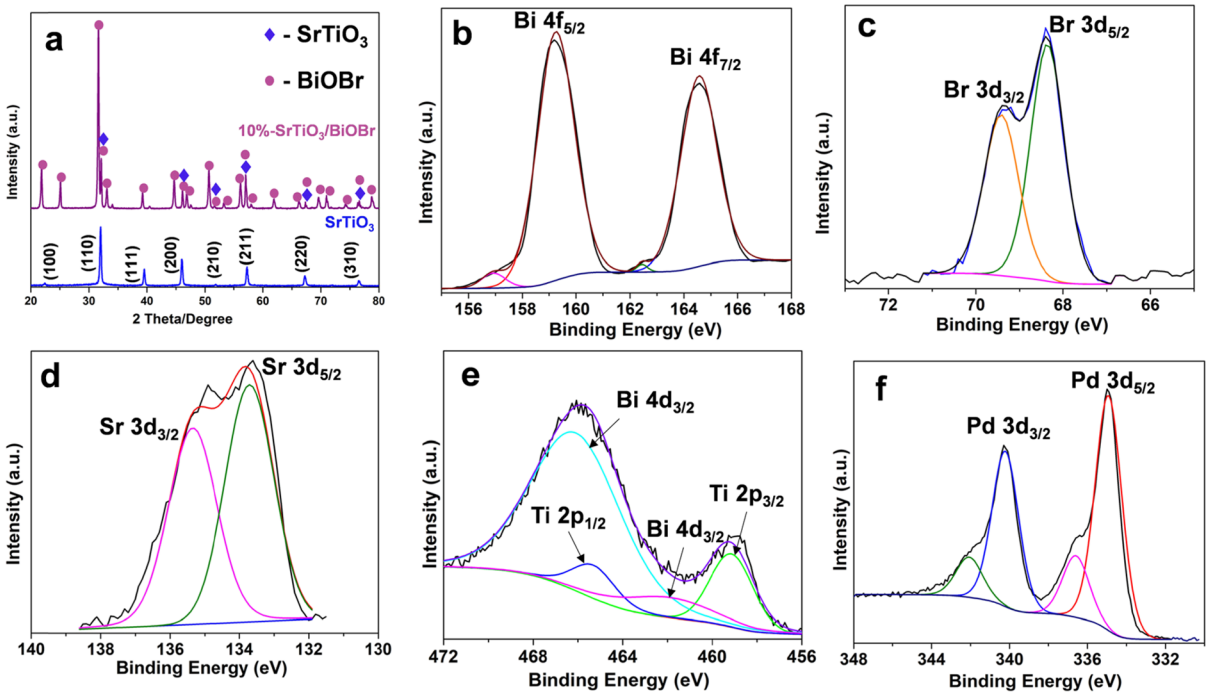

Figure 4. X-ray-based characterization of the $SrTiO_3$/BiOBr/Pd materials. Part (a) presents the powder XRD diffraction pattern, while parts (b–f) present the high-resolution XPS analysis results for (b) Bi, (c) Br, (d) Sr, (e) Ti, and (f) Pd.

Figure 4b–f confirms the presence of Sr, Ti, Bi, Br, and Pd in the material. Deconvoluted peaks of Bi^{3+} were identified at binding energies of 159.2 and 164.6 eV for Bi $4f_{5/2}$ and $4f_{7/2}$, respectively (Figure 4b). Figure 4c,d shows the deconvoluted peaks for Br^- at 68.3 and 69.3 eV for the Br $3d_{5/2}$ and Br $3d_{3/2}$ peaks respectively, while the presence of Sr^{2+} is indicated with binding energies at 133.5 and 134.8 eV for the Sr $3d_{5/2}$ and Sr $3d_{3/2}$ peaks, respectively. The deconvoluted plot for Ti^{4+} was confirmed with binding energies of 459.2 and 465.5 eV arising from the Ti $2p_{3/2}$ and $2p_{1/2}$ peaks, respectively (Figure 4e). Note that the Bi $4d_{3/2}$ peaks overlap with the Ti $2p_{1/2}$ peak, which is demonstrated in Figure 4e.[29] Finally, Figure 4f presents the deconvoluted peaks for Pd^0 from the Pd metal nanoparticles with binding energies at 334 eV for the Pd $3d_{5/2}$ peak and 340 eV for the $3d_{3/2}$ peak. From this analysis, 80% of the Pd composite was Pd^0, while 20% was PdO. PdO peaks were observed at 336.6 eV (Pd $3d_{5/2}$) and 342 eV (Pd $3d_{3/2}$).

Additional characterization of the optical properties of the $SrTiO_3$/BiOBr/Pd materials was completed using UV–vis DRS analysis (Supporting Information, Figure S2). For the $SrTiO_3$ bare materials, an absorption edge was observed at 372 nm. Analysis of the $SrTiO_3$/BiOBr materials revealed an absorption edge at 400 nm, indicating that visible light is more efficient for activating the heterojunction composite for reactivity. From these absorption edges, the band gaps of the materials were estimated to be 3.3 eV for $SrTiO_3$ and 3.1 eV for $SrTiO_3$/BiOBr, which were determined using standard Kubelka–Munk transformations.[30] Note that UV–vis DRS analysis of the final $SrTiO_3$/BiOBr/Pd structures was not completed as incorporation of the noble metal particles is not anticipated to result in any optical changes.

Photocatalytic Activity. With confirmation of the heterojunction structure, the reactivity of the $SrTiO_3$/BiOBr materials with and without Pd was analyzed via the

https://doi.org/10.1021/acs.langmuir.1c01537
Langmuir 2021, 37, 11986–11995

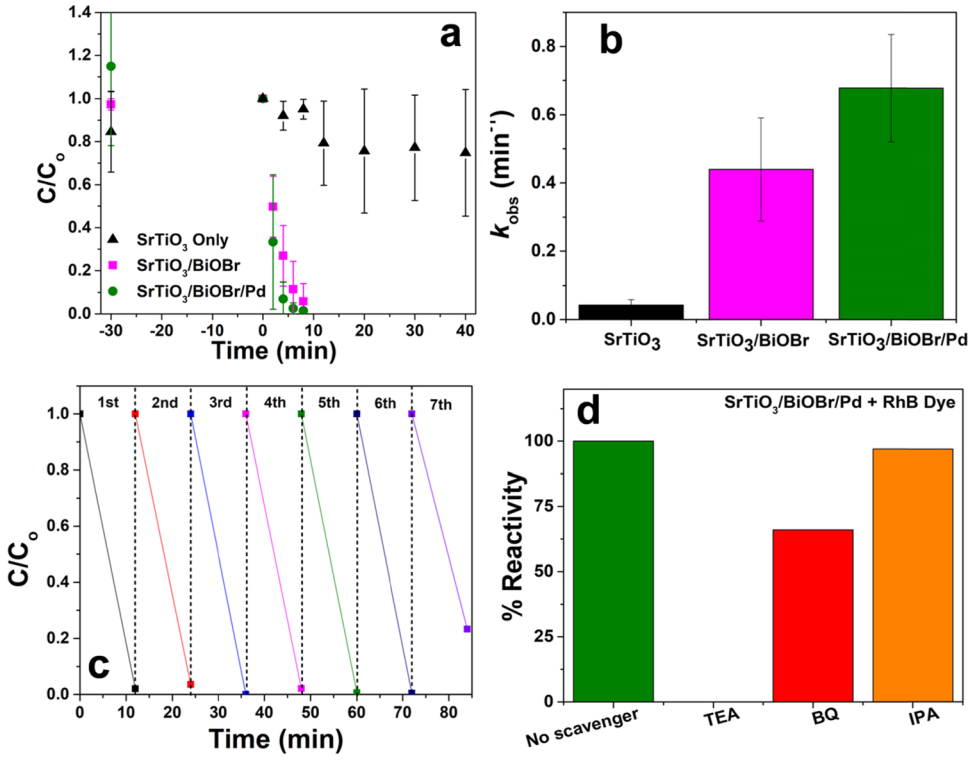

Figure 5. Photocatalytic analysis of the $SrTiO_3$/BiOBr/Pd materials for RhB degradation. Part (a) presents the catalytic analysis results as a function of time, while part (b) compares the k_{obs} values of the indicated materials. The recyclability analysis result of the catalytic materials is presented in part (c), and part (d) presents the scavenger analysis results for the reaction.

photocatalytic degradation of a variety of model organic pollutants. Such catalytic processes are extremely important for environmental remediation where the application of visible light remains challenging to achieve. Visible-light photocatalytic degradation is ideal to exploit the entire solar spectrum for irradiation for sustainable degradation of persistent organic pollutants. For this analysis, photocatalytic decomposition of both colored (RhB and methylene blue (MB) dyes) and colorless (phenol and nitrobenzene) substrates was examined. In these initial studies, the ability to degrade the compounds was examined using the newly developed heterojunction materials; future studies will focus on elucidating the overall catalytic breakdown mechanism to identify intermediates and final products. For the photocatalytic experiments, the catalyst ($SrTiO_3$/BiOBr or $SrTiO_3$/BiOBr/Pd) was dispersed in an aqueous solution of the substrate. The mixture was sonicated for 3 min and stirred in the dark for 30 min before irradiating with simulated solar light with a UV cut off filter that blocks all light with wavelengths of <400 nm. This incubation period was due to substrate adsorption, which was completed within this time frame. The reaction was monitored via extraction of aliquots taken at different time points, which were subsequently quantified using appropriate techniques (e.g., UV−vis for dyes and HPLC or GC−MS for colorless substrates).

Figure 5 presents the analysis for the degradation of RhB dye. Figure 5a specifically presents substrate degradation over time using the indicated semiconductor photocatalyst. Note that the substrate was allowed to equilibrate with the surface of the inorganic materials for 30 min (negative time points in the graph), where the sample was irradiated at time = 0 min. Upon irradiation, rapid dye degradation was observed where reaction completion was reached within 6 min for the $SrTiO_3$/BiOBr/Pd catalysts and within 10 min for the Pd-free $SrTiO_3$/BiOBr structures. From this analysis, the pseudo-first-order rate constants of the reaction (k_{obs}) can be calculated, giving rise to values of 0.44 ± 0.15 and 0.68 ± 0.16 min^{-1} for the $SrTiO_3$/BiOBr and $SrTiO_3$/BiOBr/Pd photocatalysts, respectively (Figure 5b). As a control, the photocatalytic reactivity of the $SrTiO_3$ materials without BiOBr or Pd was examined using the same reaction conditions. As anticipated, negligible reactivity was observed where only 25% of the dye degraded after 40 min of irradiation (k_{obs} = 0.043 ± 0.016 min^{-1}), confirming the effect of the heterojunction in enhancing the reactivity.

The reactivity of the materials for RhB photocatalytic degradation was noted to be highly recyclable. Recyclability studies were performed using $SrTiO_3$/BiOBr/Pd over seven consecutive photocatalytic cycles. As shown in Figure 5c, complete degradation of RhB dye was observed over six reaction cycles in 10 min; however, 78% of the dye was degraded over the same time frame during the seventh reaction cycle. This suggests that the materials were highly reactive over multiple reaction cycles, but after extended use, regeneration of the materials may be required due to a slight decrease in reactivity. To measure the efficiency of the reaction to mineralize the RhB dye, TOC analysis was completed on the reaction catalyzed using the $SrTiO_3$/BiOBr/Pd materials (Figure S3). In this system, 3.8% of the RhB was mineralized; however, all of the RhB was degraded. This suggests that intermediates were generated, which will be fully examined to identify reaction pathways in future studies.[31,32]

With confirmation of the reactivity, recyclability, and heterojunction structural effects, radical scavengers were exploited to identify key reaction species involved in the photocatalytic process. For this analysis, triethanolamine (TEA), benzoquinone (BQ), and isopropyl alcohol (IPA)

https://doi.org/10.1021/acs.langmuir.1c01537
Langmuir 2021, 37, 11986−11995

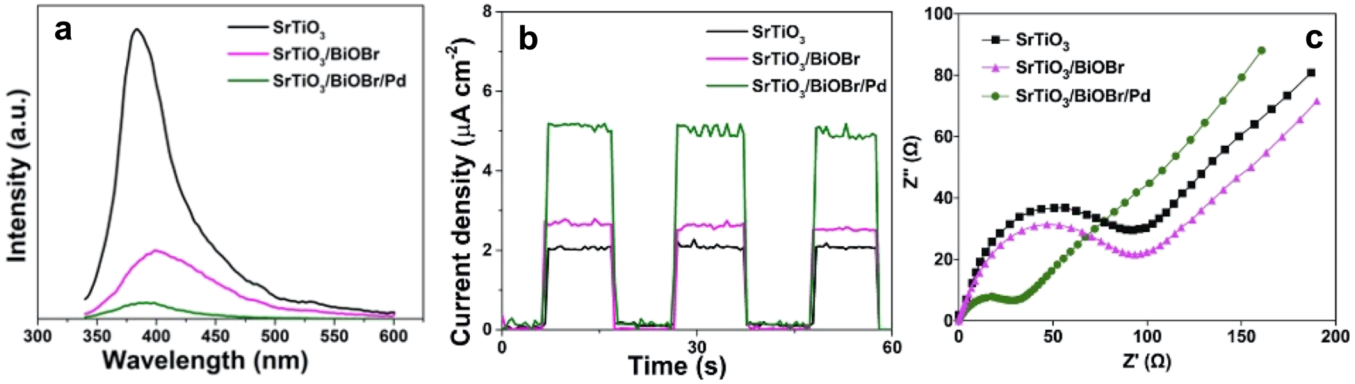

Figure 6. Photoluminescence and electrochemical analysis of charge recombination for the $SrTiO_3$/BiOBr/Pd materials. Part (a) presents the photoluminescence analysis result of the materials, part (b) displays the photocurrent measurement results, and part (c) shows the Nyquist plot for the EIS analysis.

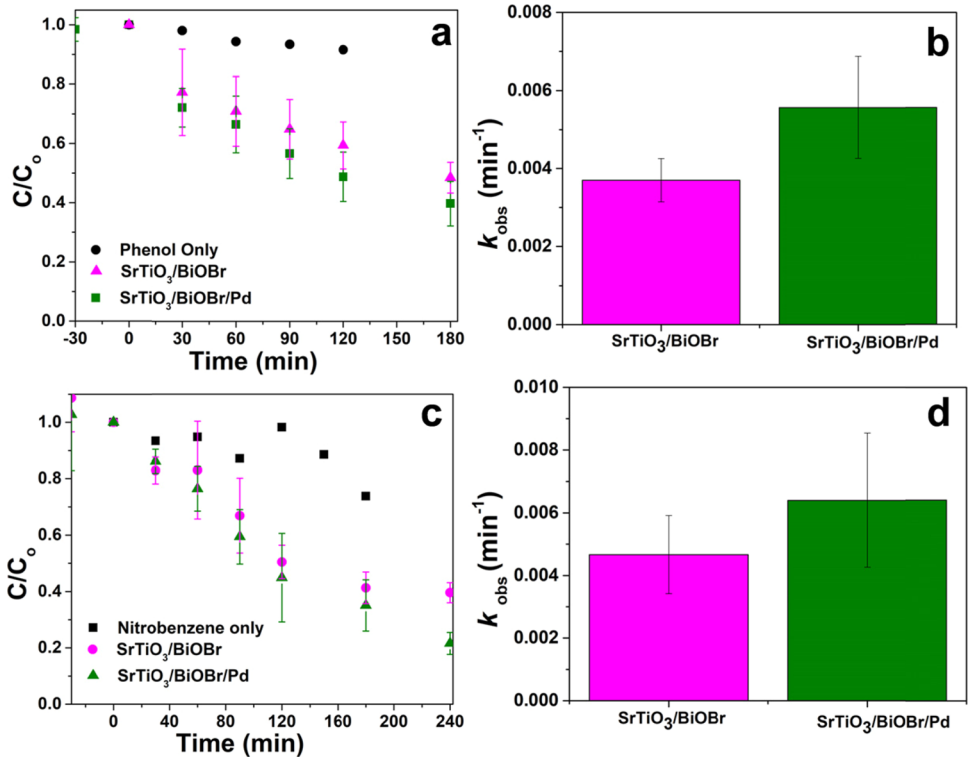

Figure 7. Photocatalytic analysis of the $SrTiO_3$/BiOBr/Pd materials for the degradation of (a and b) phenol and (c and d) nitrobenzene. Parts (a and c) present the substrate degradation as a function of time, while parts (b and d) compare the k_{obs} values.

were introduced into the RhB photocatalytic degradation process catalyzed by $SrTiO_3$/BiOBr/Pd to scavenge holes (h^+), superoxide radicals ($^{\cdot}O_2^-$), and hydroxyl radicals ($^{\cdot}OH$), respectively. As shown in Figure 5d, the reactivity decreased by 100% using TEA, 34% in the presence of BQ, and 3% with IPA as compared to the scavenger-free reaction. This suggests that holes are the dominant species for the dye degradation process followed by $\cdot O_2^-$ playing a notable role. Interestingly, while $^{\cdot}OH$ may facilitate RhB degradation, its effect was negligible as compared to the other species.

To further evaluate the photocatalytic reactivity of the metal oxide composites, the light-catalyzed degradation of MB dye was monitored, as shown in the Supporting Information, Figure S4. Using the Pd-free heterojunction, $SrTiO_3$/BiOBr, the material degraded 76% of the dye within 60 min, giving rise to a k_{obs} value of 0.023 ± 0.009 min^{-1}. When the $SrTiO_3$/BiOBr/Pd system was employed under the same conditions, 90% of the MB was consumed over the 60 min reaction time with a higher k_{obs} value of 0.037 ± 0.001 min^{-1}.

When comparing the two photocatalytic dye degradation studies, two key points are evident: (1) enhanced reactivity was observed from the $SrTiO_3$/BiOBr/Pd materials, and (2) differences in reaction rates were present based upon the substrate (RhB vs MB). For the latter point, changes in reactivity are anticipated due to the energy levels (LUMO) of both dyes. When comparing the reactivities between the two dyes, $SrTiO_3$/BiOBr/Pd degraded RhB 18 times faster than MB. Chang et al. reported a higher RhB dye degradation compared to MB and methyl orange (MO) due to the different LUMO levels of the dyes.[33] RhB possessed a higher LUMO of −2.207 eV compared with −3.277 and −3.553 eV for MO and MB, respectively. At a higher LUMO level, under visible light,

https://doi.org/10.1021/acs.langmuir.1c01537
Langmuir 2021, 37, 11986−11995

the electrons from the excited RhB dye can more readily transfer to the valence band of $SrTiO_3$/BiOBr/Pd compared to MB dye with a lower energy LUMO. This suggests that there is a direct correlation between the dye LUMO and their ability to be degraded.

Beyond the difference in molecular structure, enhanced reactivity was clearly evident from the Pd-containing $SrTiO_3$/BiOBr/Pd materials as compared to the Pd-free heterojunction. This is anticipated to arise from enhanced charge separation, facilitating the photocatalytic reactivity. To confirm this effect, photoluminescence (PL) and electrochemical studies were used to examine the rate of electron−hole pair recombination in the materials. For the PL analysis, the higher the intensity of the spectrum, the higher the recombination rate of the electron−hole pair, which also directly impacts the observed photocatalytic reactivity. Figure 6a presents the PL spectra of three specific materials: $SrTiO_3$, $SrTiO_3$/BiOBr, and $SrTiO_3$/BiOBr/Pd. As anticipated, the $SrTiO_3$ individual system has the highest peak intensity, while the ternary $SrTiO_3$/BiOBr/Pd composition has the lowest. For the Pd-free heterojunction structure, $SrTiO_3$/BiOBr, the PL intensity was intermediate between the other two material compositions. These results indicate that while the heterojunction material ($SrTiO_3$/BiOBr) has a lower charge pair recombination rate as compared to the $SrTiO_3$ itself, it is still significantly higher than the charge recombination rate for the Pd-containing $SrTiO_3$/BiOBr system. Such results are directly correlated with the observed reactivity, consistent with longer charge separation lifetimes leading to materials with enhanced photocatalytic reactivity.

Electrochemical measurements were also conducted on the $SrTiO_3$, $SrTiO_3$/BiOBr, and $SrTiO_3$/BiOBr/Pd materials. The photocurrent measurements displayed in Figure 6b examined the charge separation of the materials with and without light every 10 s for 60 s. $SrTiO_3$/BiOBr/Pd showed a higher photocurrent value compared to $SrTiO_3$/BiOBr and $SrTiO_3$, consistent with its greater photocatalytic activity. Electrochemical impedance spectroscopy (EIS) was also performed using all three of the materials, which examines the electron transfer resistance in the materials. The resistance is measured wherein the smaller the diameter of the semicircle, the lower the electron transfer resistance, indicating a higher photocatalytic activity. The Nyquist plot presented in Figure 6c shows that the $SrTiO_3$/BiOBr/Pd material has the smallest arc diameter compared to $SrTiO_3$/BiOBr and $SrTiO_3$. This is attributed to the reduction of charge transfer resistance upon loading of the Pd nanodomains, which facilitates photoinduced electron transfer, resulting in enhanced reactivity. In all cases, PL, photocurrent measurements, and EIS, enhanced charge separation lifetimes were observed for the $SrTiO_3$/BiOBr/Pd materials as compared to the $SrTiO_3$/BiOBr and $SrTiO_3$ structures, which is fully consistent with the significantly enhanced reactivity observed for the Pd-containing heterojunction.

In addition to the degradation of the colored molecular dyes, the degradation of phenol and nitrobenzene was also evaluated with the $SrTiO_3$/BiOBr-based materials, as shown in Figure 7. These two substrates were chosen as they are colorless model organic pollutants, expanding the range of substrates for degradation. Figure 7a specifically presents the degradation of phenol over time with 52 and 61% of the molecule degraded over 3 h for $SrTiO_3$/BiOBr and $SrTiO_3$/BiOBr/Pd, respectively. This resulted in k_{obs} values of $(3.7 \pm 0.6) \times 10^{-3}$ min^{-1} for $SrTiO_3$/BiOBr and $(5.6 \pm 1.3) \times 10^{-3}$ min^{-1} for $SrTiO_3$/BiOBr/Pd (Figure 7b). TOC analysis for phenol degradation using the Pd-containing heterojunction indicated that 7.7% of the substrate was mineralized over the 3 h reaction timeframe.

Finally, the degradation of nitrobenzene, a highly carcinogenic pollutant widely used in dyes, explosives, and pesticides, was also examined.[34] Figure 7c shows the photocatalytic degradation of this compound using the $SrTiO_3$/BiOBr-based materials via the oxidative process. To this end, 78% of the nitrobenzene was degraded over the 4 h reaction time using the Pd-containing $SrTiO_3$/BiOBr/Pd materials, while 61% of the substrate was decomposed using the $SrTiO_3$/BiOBr photocatalysts. From this analysis, k_{obs} values of $(6.4 \pm 2.1) \times 10^{-3}$ and $(4.7 \pm 1.3) \times 10^{-3}$ min^{-1} were calculated for the Pd-containing and Pd-free heterojunctions, respectively (Figure 7d). TOC analysis of the $SrTiO_3$/BiOBr/Pd-driven reaction indicated that 10.2% of the nitrobenzene was mineralized. As anticipated for both colorless substrates, the Pd-coated photocatalysts exhibited a higher reactivity than the uncoated metal oxide, consistent with the dye degradation studies and the electrochemical analyses.

From the photocatalytic analysis, it is evident that enhanced reactivity is observed from the heterojunction materials with Pd nanoparticles present on the surface. Based upon the PL and EIS analyses, the Pd minimizes charge pair recombination, which leads to the enhanced reactivity. This likely occurs from the electrons becoming trapped on the noble metal material, preventing recombination and facilitating $\cdot O_2^-$ production. To generate $\cdot O_2^-$, molecular oxygen abstracts the electron off the Pd surface, where the newly produced $\cdot O_2^-$ drives toxicant degradation. In addition, while the Pd sequesters the electrons, this also leaves holes present on the oxide materials, which drives toxicant oxidation. This process is one of the main driving forces for RhB degradation (Figure 5d), which is optimized in the presence of the Pd component that facilitates charge separation lifetimes.

When comparing the reactivity between the materials reported in this work and other systems that are the most comparable, enhanced reactivity is observed (see Supporting Information, Table S1, for comparison). Unfortunately, direct correlation with other $SrTiO_3$/BiOBr/Pd is not readily possible; however, other systems that varied the n-type semiconductor or lacked the Pd component can be compared. For instance, Chen et al. synthesized N-doped $SrTiO_3$/BiOBr with different weight percents of $SrTiO_3$.[35] The 18% $SrTiO_3$/BiOBr composite exhibited the highest reactivity when used to degrade RhB dye under UV light, degrading almost 100% of the dye in 60 min. When visible light was used to degrade RhB dye using the same composite, minimal reactivity was observed.[35] It is important to note, however, that UV light was not used in the present system. Kanagaraj et al. synthesized $SrTiO_3$ nanocubes and mesoporous BiOBr via a sol−gel method and a precipitation method separately.[20] A $SrTiO_3$/BiOBr composite was then synthesized from these components via an impregnation approach with different weight percents of $SrTiO_3$ in the mixture. The composite reactivities were examined by the degradation of reactive blue 198, reactive black 5, and reactive yellow 145 dyes. From the different materials studied, the 10% $SrTiO_3$/BiOBr showed the highest reactivity for the decolorization of the three dyes, where nearly 100% of reactive blue 198, reactive black 5, and reactive yellow 145 dyes were decolorized in 30, 90, and 60 min, respectively.

https://doi.org/10.1021/acs.langmuir.1c01537
Langmuir 2021, 37, 11986−11995

Such a reactivity required notably longer timeframes to reach completion compared to the present materials with the molecular dyes; however, differences in the dye substrates may affect such a reactivity.

Alternatively, Pálmai et al. synthesized a Pd-decorated ternary composite of *m*-$BiVO_4$/BiOBr for the degradation of RhB dye and other environmental pollutants. In this case, the n-type material was substituted for $BiVO_4$ instead of the $SrTiO_3$ used here. The $BiVO_4$/BiOBr/Pd composite degraded 100% of the RhB dye with a k_{obs} value of 0.534 min^{-1}, which is lower than the k_{obs} for the $SrTiO_3$/BiOBr/Pd system (0.68 min^{-1}).[24] In an additional system, Guan et al. prepared a novel $LaFeO_3$/BiOBr heterojunction photocatalyst for the photocatalytic removal of RhB dye.[36] For the photocatalytic testing, 5 mg/L RhB dye was used with 100 mg of photocatalyst. The most reactive photocatalyst reported degraded 98.2% of RhB in 30 min. When comparing to this work, a higher RhB dye concentration was used (10 mg/L) with a lower catalyst loading of 10 mg, which still showed a superior photocatalytic degradation efficiency.

CONCLUSIONS

In summary, a unique Pd-decorated $SrTiO_3$/BiOBr heterojunction was prepared by a direct precipitation method. The approach generated a highly integrated p−n heterojunction material that demonstrated enhanced photocatalytic reactivity for degradation of environmental pollutants. Of particular note, the materials were specifically activated by visible light, thus expanding their potential use via solar-light activation. The interfacial contact between $SrTiO_3$ and BiOBr reduced the charge recombination rate of the electrons and holes to enhance the photocatalytic reactivity. With Pd nanoparticles on the surface of the heterojunction, this component facilitated the electron transfer to drive the oxidative-based degradation of known environmental pollutants. Future studies are in progress focused on identifying the overall photocatalytic mechanism of the $SrTiO_3$/BiOBr/Pd materials for pollutant degradation to identify intermediate compounds generated and final products.

ASSOCIATED CONTENT

Supporting Information

The Supporting Information is available free of charge at https://pubs.acs.org/doi/10.1021/acs.langmuir.1c01537.

ICP/MS, UV−vis DRS, TOC, MB degradation analyses, and reaction comparison (PDF)

AUTHOR INFORMATION

Corresponding Author

Marc R. Knecht − *Department of Chemistry, University of Miami, Coral Gables, Florida 33146, United States; Dr. J.T. Macdonald Foundation Biomedical Nanotechnology Institute, University of Miami, Miami, Florida 33136, United States;* orcid.org/0000-0002-7614-7258; Email: knecht@miami.edu

Authors

Mary O. Olagunju − *Department of Chemistry, University of Miami, Coral Gables, Florida 33146, United States*

Elsayed M. Zahran − *Department of Chemistry, Ball State University, Muncie, Indiana 47306, United States;* orcid.org/0000-0003-3456-515X

Elnaz Zeynaloo − *Department of Chemistry, University of Miami, Coral Gables, Florida 33146, United States;* orcid.org/0000-0001-7152-5857

Dharmendra Shukla − *Department of Physics, University of Miami, Coral Gables, Florida 33146, United States*

Joshua L. Cohn − *Department of Physics, University of Miami, Coral Gables, Florida 33146, United States;* orcid.org/0000-0002-0702-9872

Bapurao Surnar − *Department of Biochemistry and Molecular Biology, Leonard M. Miller School of Medicine, University of Miami, Miami, Florida 33136, United States;* orcid.org/0000-0001-5997-3120

Shanta Dhar − *Department of Chemistry, University of Miami, Coral Gables, Florida 33146, United States; Department of Biochemistry and Molecular Biology and Sylvester Comprehensive Cancer Center, Leonard M. Miller School of Medicine, University of Miami, Miami, Florida 33136, United States;* orcid.org/0000-0003-3042-5272

Leonidas G. Bachas − *Department of Chemistry, University of Miami, Coral Gables, Florida 33146, United States; Dr. J.T. Macdonald Foundation Biomedical Nanotechnology Institute, University of Miami, Miami, Florida 33136, United States;* orcid.org/0000-0002-3308-6264

Complete contact information is available at: https://pubs.acs.org/10.1021/acs.langmuir.1c01537

Notes

The authors declare no competing financial interest.

ACKNOWLEDGMENTS

This work was supported in part by the National Science Foundation under grant 1903649 (M.R.K.). E.M.Z. acknowledges support from Ball State University. S.D. thanks Sylvester Comprehensive Cancer Center for financial support. Finally, the authors thank Professor Dennis A. Hansell and Lillan Custals for assistance with the TOC analysis.

REFERENCES

(1) Kaur, N.; Shahi, S. K.; Singh, V. Anomalous behavior of visible light active TiO_2 for the photocatalytic degradation of different Reactive dyes. *Photochem. Photobiol. Sci.* **2015**, *14*, 2024−2034.

(2) Wang, C.; Qiu, H.; Inoue, T.; Yao, Q. Band gap engineering of $SrTiO_3$ for water splitting under visible light irradiation. *Int. J. Hydrogen Energy* **2014**, *39*, 12507−12514.

(3) Han, J.; Dai, F.; Liu, Y.; Zhao, R.; Wang, L.; Feng, S. Synthesis of CdSe/$SrTiO_3$ nanocomposites with enhanced photocatalytic hydrogen production activity. *Appl. Surf. Sci.* **2019**, *467-468*, 1033−1039.

(4) Subramanian, V.; Roeder, R. K.; Wolf, E. E. Synthesis and UV−visible-light photoactivity of noble-metal−$SrTiO_3$ composites. *Ind. Eng. Chem. Res.* **2006**, *45*, 2187−2193.

(5) Shafafi, S.; Habibi-Yangjeh, A.; Feizpoor, S.; Ghosh, S.; Maiyalagan, T. Carbon dots and $Bi_4O_5Br_2$ adhered on TiO_2 nanoparticles: Impressively boosted photocatalytic efficiency for removal of pollutants under visible light. *Sep. Purif. Technol.* **2020**, *250*, No. 117179.

(6) Cao, T.; Li, Y.; Wang, C.; Shao, C.; Liu, Y. A facile in situ hydrothermal method to $SrTiO_3$/TiO_2 nanofiber heterostructures with high photocatalytic activity. *Langmuir* **2011**, *27*, 2946−2952.

(7) Janotti, A.; Jalan, B.; Stemmer, S.; van de Walle, C. G. Effects of doping on the lattice parameter of $SrTiO_3$. *Appl. Phys. Lett.* **2012**, *100*, 262104.

(8) Tan, C.-E.; Lee, J.-T.; Su, E.-C.; Wey, M.-Y. Facile approach for Z-scheme type Pt/g-$C3N_4$/$SrTiO_3$ heterojunction semiconductor synthesis via low-temperature process for simultaneous dyes

degradation and hydrogen production. *Int. J. Hydrogen Energy* **2020**, *45*, 13330−13339.
(9) Mu, L.; Zhao, Y.; Li, A.; Wang, S.; Wang, Z.; Yang, J.; Wang, Y.; Liu, T.; Chen, R.; Zhu, J.; Fan, F.; Li, R.; Li, C. Enhancing charge separation on high symmetry $SrTiO_3$ exposed with anisotropic facets for photocatalytic water splitting. *Energy Environ. Sci.* **2016**, *9*, 2463−2469.
(10) Faisal, M.; Harraz, F. A.; Ismail, A. A.; El-Toni, A. M.; Al-Sayari, S. A.; Al-Hajry, A.; Al-Assiri, M. S. Polythiophene/mesoporous $SrTiO_3$ nanocomposites with enhanced photocatalytic activity under visible light. *Sep. Purif. Technol.* **2018**, *190*, 33−44.
(11) Yue, X.; Zhang, J.; Yan, F.; Wang, X.; Huang, F. A situ hydrothermal synthesis of $SrTiO_3/TiO_2$ heterostructure nanosheets with exposed (001) facets for enhancing photocatalytic degradation activity. *Appl. Surf. Sci.* **2014**, *319*, 68−74.
(12) Iwashina, K.; Kudo, A. Rh-doped $SrTiO_3$ photocatalyst electrode showing cathodic photocurrent for water splitting under visible-light irradiation. *J. Am. Chem. Soc.* **2011**, *133*, 13272−13275.
(13) Zhang, Q.; Huang, Y.; Xu, L.; Cao, J.-J.; Ho, W.; Lee, S. C. Visible-light-active plasmonic Ag−$SrTiO_3$ nanocomposites for the degradation of NO in air with high selectivity. *ACS Appl. Mater. Interfaces* **2016**, *8*, 4165−4174.
(14) Ha, M. N.; Zhu, F.; Liu, Z.; Wang, L.; Liu, L.; Lu, G.; Zhao, Z. Morphology-controlled synthesis of $SrTiO_3/TiO_2$ heterostructures and their photocatalytic performance for water splitting. *RSC Adv.* **2016**, *6*, 21111−21118.
(15) Ji, W.; Rui, Z.; Ji, H. Z-scheme $Ag_3PO_4/Ag/SrTiO_3$ heterojunction for visible-light induced photothermal synergistic VOCs degradation with enhanced performance. *Ind. Eng. Chem. Res.* **2019**, *58*, 13950−13959.
(16) Kong, J.; Rui, Z.; Liu, S.; Liu, H.; Ji, H. Homeostasis in CuxO/$SrTiO_3$ hybrid allows highly active and stable visible light photocatalytic performance. *Chem. Commun.* **2017**, *53*, 12329−12332.
(17) Zhang, K.; Liu, C.; Huang, F.; Zheng, C.; Wang, W. Study of the electronic structure and photocatalytic activity of the BiOCl photocatalyst. *Appl. Catal. B* **2006**, *68*, 125−129.
(18) Wang, Z.; Chu, Z.; Dong, C.; Wang, Z.; Yao, S.; Gao, H.; Liu, Z.; Liu, Y.; Yang, B.; Zhang, H. Ultrathin BiOX (X = Cl, Br, I) nanosheets with exposed {001} facets for photocatalysis. *ACS Appl. Nano Mater.* **2020**, *3*, 1981−1991.
(19) Wang, Y.; Shi, Z.; Fan, C.; Wang, X.; Hao, X.; Chi, Y. Synthesis, characterization, and photocatalytic properties of BiOBr catalyst. *J. Solid State Chem.* **2013**, *199*, 224−229.
(20) Kanagaraj, T.; Thiripuranthagan, S. Photocatalytic activities of novel $SrTiO_3$ − BiOBr heterojunction catalysts towards the degradation of reactive dyes. *Appl. Catal. B* **2017**, *207*, 218−232.
(21) Xia, Y.; He, Z.; Su, J.; Liu, Y.; Tang, B. Fabrication and photocatalytic property of novel $SrTiO_3/Bi_5O_7I$ nanocomposites. *Nanoscale Res. Lett.* **2018**, *13*, 148.
(22) Ashiri, R.; Moghtada, A. Carbonate-free Strontium Titanium Oxide nanosized crystals with tailored morphology: facile synthesis, characterization, and formation mechanism. *Metall Mater. Trans. B* **2014**, *45*, 1979−1986.
(23) Xu, M.; Lu, Y.-N.; Liu, Y.-F.; Shi, S.-Z.; Fang, F. Synthesis of Monosized Strontium Titanate Particles with Tailored Morphologies. *J. Am. Ceram. Soc.* **2006**, *89*, 3631−3634.
(24) Pálmai, M.; Zahran, E. M.; Angaramo, S.; Bálint, S.; Pászti, Z.; Knecht, M. R.; Bachas, L. G. Pd-decorated m-$BiVO_4$/BiOBr ternary composite with dual heterojunction for enhanced photocatalytic activity. *J. Mater. Chem. A* **2017**, *5*, 529−534.
(25) Abdi, M.; Mahdikhah, V.; Sheibani, S. Visible light photocatalytic performance of La-Fe co-doped $SrTiO_3$ perovskite powder. *Opt. Mater.* **2020**, *102*, No. 109803.
(26) Gong, C.; Chu, J.; Qian, S.; Yin, C.; Hu, X.; Wang, H.; Wang, Y.; Ding, X.; Jiang, S.; Li, A.; Gong, Y.; Wang, X.; Li, C.; Zhai, T.; Xiong, J. Large-scale ultrathin 2D wide-bandgap BiOBr nanoflakes for gate-controlled deep-ultraviolet phototransistors. *Adv. Mater.* **2020**, *32*, No. 1908242.
(27) Olagunju, M. O.; Poole, X.; Blackwelder, P.; Thomas, M. P.; Guiton, B. S.; Shukla, D.; Cohn, J. L.; Surnar, B.; Dhar, S.; Zahran, E. M.; Bachas, L. G.; Knecht, M. R. Size-controlled $SrTiO_3$ nanoparticles photodecorated with Pd cocatalysts for photocatalytic organic Dye degradation. *ACS Appl. Nano Mater.* **2020**, *3*, 4904−4912.
(28) Olagunju, M. O.; Zahran, E. M.; Reed, J. M.; Zeynaloo, E.; Shukla, D.; Cohn, J. L.; Surnar, B.; Dhar, S.; Bachas, L. G.; Knecht, M. R. Halide effects in $BiVO_4$/BiOX heterostructures decorated with Pd nanoparticles for photocatalytic degradation of Rhodamine B as a model organic pollutant. *ACS Appl. Nano Mater.* **2021**, *4*, 3262.
(29) Hou, D.; Hu, X.; Wen, Y.; Shan, B.; Hu, P.; Xiong, X.; Qiao, Y.; Huang, Y. Electrospun sillenite $Bi_{12}MO_{20}$ (M = Ti, Ge, Si) nanofibers: general synthesis, band structure, and photocatalytic activity. *Phys. Chem. Chem. Phys.* **2013**, *15*, 20698−20705.
(30) George, P.; Chowdhury, P. Complex dielectric transformation of UV-vis diffuse reflectance spectra for estimating optical band-gap energies and materials classification. *Analyst* **2019**, *144*, 3005−3012.
(31) Cui, Y.; Sun, H.; Shen, G.; Jing, P.; Pu, Y. Effect of dual-cocatalyst surface modification on photodegradation activity, pathway, and mechanisms with highly efficient Ag/$BaTiO_3$/MnOx. *Langmuir* **2020**, *36*, 498−509.
(32) Yu, K.; Yang, S.; He, H.; Sun, C.; Gu, C.; Ju, Y. Visible light-driven photocatalytic degradation of Rhodamine B over $NaBiO_3$: pathways and mechanism. *J. Phys. Chem. A* **2009**, *113*, 10024−10032.
(33) Chang, X.; Gondal, M. A.; Al-Saadi, A. A.; Ali, M. A.; Shen, H.; Zhou, Q.; Zhang, J.; Du, M.; Liu, Y.; Ji, G. Photodegradation of Rhodamine B over unexcited semiconductor compounds of BiOCl and BiOBr. *J. Colloid Interface Sci.* **2012**, *377*, 291−298.
(34) Sun, Y.; Yang, Z.; Tian, P.; Sheng, Y.; Xu, J.; Han, Y.-F. Oxidative degradation of nitrobenzene by a Fenton-like reaction with Fe-Cu bimetallic catalysts. *Appl. Catal. B* **2019**, *244*, 1−10.
(35) Chen, L.; Shi, L.; Wu, J.; Tong, Z.; Huang, C.; Li, C.; Ou, B.; Peng, C.; Tian, L.; Tang, J. N-$SrTiO_3$ nanoparticle/BiOBr nanosheet as 0D/2D heterojunctions for enhanced visible light photocatalytic dye degradation. *Mater. Sci. Eng.: B* **2020**, *261*, No. 114667.
(36) Guan, S.; Yang, H.; Sun, X.; Xian, T. Preparation and promising application of novel $LaFeO_3$/BiOBr heterojunction photocatalysts for photocatalytic and photo-Fenton removal of dyes. *Opt. Mater.* **2020**, *100*, No. 109644.

https://doi.org/10.1021/acs.langmuir.1c01537
Langmuir 2021, 37, 11986−11995